

# How Is Diffusion of Neutral and Charged Tracers Related to the Structure and Dynamics of a Room-Temperature Ionic Liquid? Large Deviations from Stokes–Einstein Behavior Explained

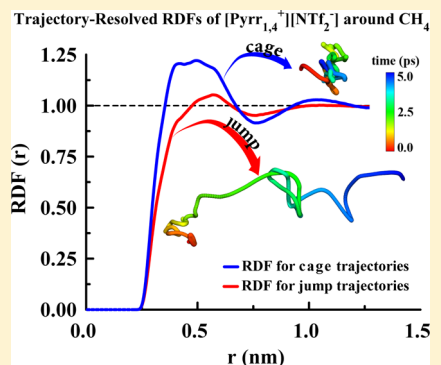
Juan C. Araque,<sup>†</sup> Sharad K. Yadav,<sup>†</sup> Michael Shadeck,<sup>‡</sup> Mark Maroncelli,<sup>‡</sup> and Claudio J. Margulis\*,<sup>†</sup>

<sup>†</sup>Department of Chemistry, University of Iowa, Iowa City, Iowa 52242, United States

<sup>‡</sup>Department of Chemistry, The Pennsylvania State University, University Park, Pennsylvania 16802, United States

## Supporting Information

**ABSTRACT:** The deviations from Stokes–Einstein hydrodynamics of small solutes are more pronounced in ionic liquids than in conventional solvents (*J. Phys. Chem. B* 2013 **117** (39), 11697). Small neutral solutes diffuse much faster than expected, whereas small charged solutes diffuse much slower. This article attempts to establish a link between the local friction experienced by tracer solutes and the polar/apolar structure of ionic liquids. We find that small neutral solutes probe locally “stiff” (mostly charged, high electrostriction) regions and locally “soft” (mostly apolar, low electrostriction) regions. These regions of high and low friction are associated with cage and jump regimes. Enhanced neutral tracer mobility in the low friction regions associated with the cationic apolar component has an important bearing on the large positive deviations from Stokes–Einstein behavior. In contrast, diminished charged tracer mobility involves long caging dynamics separated by jump events often triggered by the loss and recovery of counterions.



## 1. INTRODUCTION

A deeper mechanistic understanding of the diffusion process in the case of charged and neutral tracers in modern ionic liquids (ILs) is desirable because it is at the core of numerous technological areas such as charge transport for energy conversion or storage devices,<sup>1–3</sup> diffusion of reactants and intermediates in homogeneously catalyzed reactions,<sup>4–7</sup> or selective recovery of solutes in liquid–liquid extraction processes.<sup>8,9</sup>

When the size ratio between the solute and solvent is small, the detailed liquid landscape becomes relevant and deviations from Stokes–Einstein (SE) behavior apparent.<sup>10</sup> Experimental evidence is available in common solvents,<sup>11</sup> polymers,<sup>12,13</sup> and supercooled liquids.<sup>14</sup> This phenomenon becomes extreme in the case of ILs<sup>15–17</sup> because the liquid landscape is often heterogeneous and friction, normally a property of the solvent, becomes dependent on the charge of the solute and its location. One example of such anomalous behavior occurs in bimolecular electron transfer reactions. In ILs, it has been experimentally found that if reactant species are small and neutral, rates are anomalously high,<sup>5,18–24</sup> whereas if they are charged, reactions are anomalously slow.<sup>25–28</sup> Here anomalous refers to a comparison with what would be expected from theories that assume friction is independent of the solute charge and the same everywhere in the solvent.

The current work attempts to provide mechanistic insight into intriguing phenomena depicted in Figure 1. In Figure 1b, the blue and red lines are fits of the ratio between the observed and SE predicted friction (defined in eq 1) to an extensive set

of experimental tracer diffusion data, derived from a wide variety of experimental data collected in refs 15 and 16. Open circles correspond to values derived in the current work from molecular dynamics (MD) simulations and filled circles from NMR measurements of different solutes, all in 1-butyl-1-methylpyrrolidinium bis(trifluoromethanesulfonyl)imide ( $[\text{Pyrr}_{4,1}^+][\text{NTf}_2^-]$ ). SE behavior occurs for both neutral and charged solutes in the limit of large solute to solvent volume ratio  $V_u/V_v$ , but when this ratio is smaller than one, significant deviations occur.

$$\frac{\zeta_{\text{obs}}}{\zeta_{\text{SE}}} = \frac{D_{\text{SE}}}{D_{\text{obs}}} = \frac{k_B T / 6\pi\eta_{\text{obs}} R_{\text{solute}}}{D_{\text{obs}}} \quad (1)$$

We will show that in the case of small neutral solutes diffusion is likely not dominated by solute–solvent interactions but instead by solvent–solvent interactions. Because of the polar/apolar nature of the solvent, small neutral tracers sample regions that are stiff, where solvent–solvent friction is high and regions that are soft where it is low. Neutral tracer mobility is therefore enhanced by diffusion through the soft regions of the liquid. Stiff and soft solvent locations naturally correlate with the polar or apolar components of the medium. Soft, mostly apolar solvation plays a defining role on the faster than expected diffusion of neutral tracers.

**Received:** February 2, 2015

**Revised:** March 24, 2015

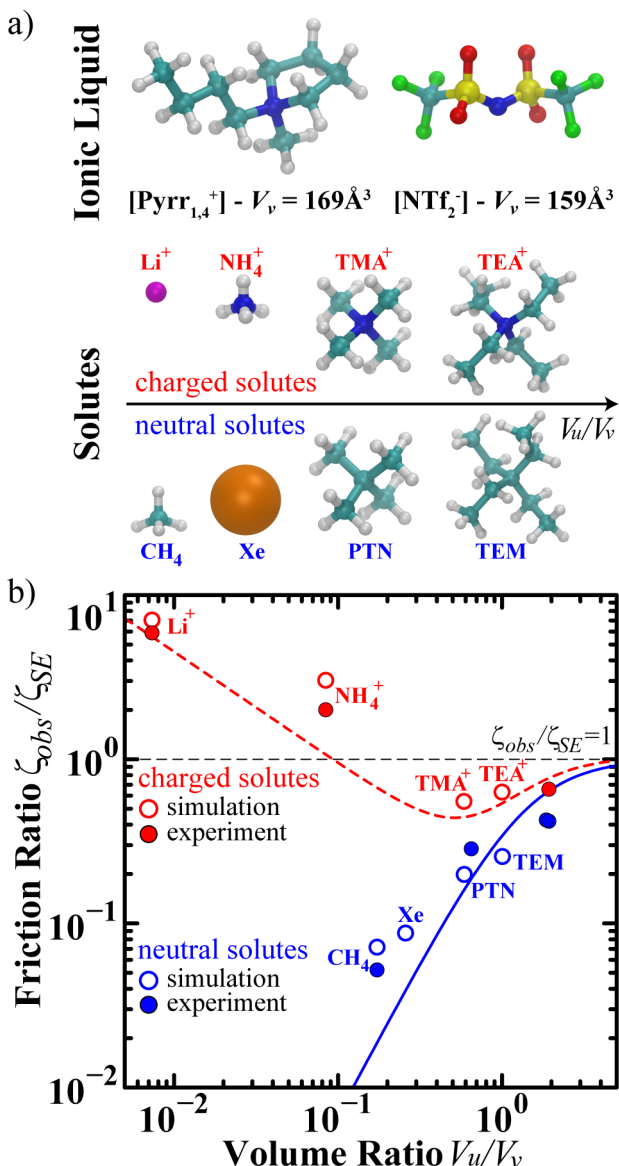


**Figure 1.** (a) Schematic representation of: (top) molecular structure of the neat IL constituents 1-butyl-1-methylpyrrolidinium cation  $[\text{Pyrr}_{4,1}^+]$  and bis(trifluoromethanesulfonyl)imide anion  $[\text{NTf}_2^-]$  and (bottom) molecular structure of the solutes considered ordered according to their molecular volumes and classified as neutral or charged. The color coding of the atoms is as follows: carbon, cyan; hydrogen, white; nitrogen, blue; oxygen, red; sulfur, yellow; fluorine, green. (b) Translational friction ratio,  $\zeta_{\text{obs}}/\zeta_{\text{SE}}$  for spherical and quasi-spherical solutes with either neutral or positive (+1) charge. Comparison is between MD simulation estimates (at 400 K) and experimental data from current work (at 298 K), except data for Li<sup>+</sup> in  $[\text{Pyrr}_{4,1}^+][\text{NTf}_2^-]$  at 303 K, which is from ref 29. Blue and red lines are fits to diffusion NMR data in ILs from refs 15 and 16:  $(\zeta_{\text{obs}}/\zeta_{\text{SE}})_{\text{neutral}} = \{1 + 1.93(V_u/V_v)^{-1.88}\}^{-1}$  for dilute neutral solutes and  $(\zeta_{\text{obs}}/\zeta_{\text{SE}})_{\pm 1} = (\zeta_{\text{obs}}/\zeta_{\text{SE}})_{\text{neutral}} + 0.198(V_u/V_v)^{-0.679}$  for dilute charged ( $\pm 1$ ) species, respectively. All volumes are computed using the method described in ref 30 and are listed in Tables S3 and S4 in the Supporting Information. For clarity, not all experimental tracer data points are labeled; actual experimental and computational friction values are provided in the same Tables.

In contrast, the large positive deviations in the case of small charged solutes are correlated with strong caging that results in an enlarged hydrodynamic radius of the tracer. Put in a

different way, the tracer is at all times an intrinsic part of the IL charge network. On average, a small charged solute will experience significantly higher friction than would be expected by the macroscopic viscosity; therefore, diffusion is retarded.

## 2. METHODOLOGY

In the present study we consider dilute solutions of spherical (single atom/ion) and quasi-spherical (tetrahedral symmetry) solutes. The rationale for this choice is to avoid undesirable rotational-translational coupling as well as to diminish to some extent the effect of dipolar and other multipolar interactions. As the solvent, we have selected 1-butyl-1-methylpyrrolidinium bis(trifluoromethanesulfonyl)imide  $[\text{Pyrr}_{4,1}^+][\text{NTf}_2^-]$  because substantial experimental and computational structural data are available<sup>31,32</sup> which shows there is no first sharp diffraction peak in this liquid. The absence of a first sharp diffraction peak or prepeak is indicative of an absence of preformed apolar regions separated by charged regions.<sup>33,34</sup> Work on the mechanisms of diffusion in systems where there is a prepeak indicative of polarity alternation will be the subject of a future publication. As we will show later, the absence of a polarity alternation prepeak does not preclude preferential diffusion in regions that are mostly polar or mostly apolar.

The molecular structure of all tracers as well as the solvent is schematically depicted in Figure 1a. As can be seen from parts a and b of Figure 1, the chosen combination of solutes and solvent results in sampling of  $V_u/V_v$  in the full relevant range between 0.08 to 1.0.

In our simulations both the solvent and solutes are represented at the all-atom level. A list of the sources of force field parameters is given in Table S1 of the Supporting Information (SI). Model parameters for bonded and non-bonded interactions were chosen according to the OPLS-AA<sup>35</sup> prescription.

As can be seen from Table S1 in the SI, the  $[\text{Pyrr}_{4,1}^+]$  potential is derived from the Canongia Lopes and Padua (CLP)<sup>36,37</sup> parameters, whereas the  $[\text{NTf}_2^-]$  parameters are those of Köddermann, Paschek, and Ludwig (KPL).<sup>38</sup> The latter parametrization has been shown to provide a much better description of transport properties without resorting to the typical method of charge scaling.<sup>39</sup> Such improvement was achieved by fine-tuning both Lennard-Jones parameters ( $\epsilon_{ij}$  and  $\sigma_{ij}$ ) while leaving the CLP partial atomic charges unmodified.<sup>38</sup> Data presented in Figure S1 in the SI show that this combined CLP(cation)-KPL(anion) formulation gives a 2-fold deviation of the calculated diffusion coefficients ( $D_s^+$  and  $D_s^-$ ) from experimental values at 303 K,<sup>40</sup> whereas a 20-fold deviation is obtained using CLP with charges scaled by 80% and a 40-fold deviation using the original CLP with full charges. We show in Figures S2 and S3 in the SI that these parameters acceptably reproduce the liquid structure factor and the viscosity when compared with experiment.

The study of dynamical properties of tracer molecules has always been problematic because simulations must be performed at low enough solute concentrations such that solvent properties are minimally altered but statistics are sufficient so that average results are meaningful. In the case of our studies the tracer concentration was set at  $\sim 100$  mM, which is only twice the experimental value used in the NMR refs 24 and 15. In all cases, 10 tracer solutes were simulated in a box of 343 solvent ion pairs. When simulating the positively charged solutes (seen in Figure 1a), an equal number of “extra”  $[\text{NTf}_2^-]$  anions were included to maintain charge neutrality.

$[\text{Pyrr}_{4,1}^+][\text{NTf}_2^-]$  has an experimental viscosity of 74 cP at 298 K, whereas it is  $\sim$ 4.5 cP at 400 K.<sup>24</sup> Because higher ionic mobilities provide better statistics for all of our calculations, we decided to carry out all of our production runs at 400 K. Simulated viscosities for the neat liquid and solute systems are provided in Table S2 of the SI.

Two types of production runs are needed for the mechanistic studies described here. Constant temperature and volume (*NVT*) calculations are required to properly determine the liquid viscosities needed in the accurate calculation of the SE friction (eq 1). Constant energy and volume (*NVE*) calculations are instead required to estimate diffusion constants that are not spuriously contaminated by the effect of thermostats and barostats. All of our simulations were performed using the GROMACS MD package,<sup>41,42</sup> version 4.5.5, at the double-precision level. Equations of motions were integrated using a leapfrog algorithm<sup>43</sup> with a time step of 1 fs during equilibration and with a 2 fs step during long production runs. The size of our cubic simulations boxes ranged between 5.7 and 5.9 nm depending on the system, and in all cases periodic boundary conditions were applied in all three dimensions. Nonbonded pair interactions were considered using the minimum image convention with van der Waals and Coulomb (real-space sum) cutoff radii of 1.50 nm during equilibration and switch/cutoff radii of 1.18/1.20 nm during production. Longer ranged electrostatic forces and energies beyond the specified cutoff were calculated with the particle mesh Ewald (PME) method<sup>44,45</sup> with B-spline interpolation of order six and fourierspacing parameter set to 0.08-(equilibration)/0.12(production) nm. The accuracy of the reciprocal space sum, both during equilibration and production, was kept by assigning a tolerance level of  $1 \times 10^{-5}$  to the real-space electrostatic interaction at the cutoff distance. Additionally, all covalent bonds involving hydrogen atoms were constrained to their equilibrium values using the linear constraint solver (LINCS) algorithm.<sup>46,47</sup>

A careful equilibration protocol was followed to ensure proper sampling of transport properties during production runs. We began our simulations from a lattice. Solute molecules were then interdispersed within the IL crystal to achieve the prescribed concentration. This initial setup was energy-minimized using the steepest descent algorithm. The system was then simulated at 0, 10, and 100% charges in the *NpT* ensemble. During this last step a temperature-annealing protocol was implemented that raised the temperature to 500 K and lowered it back to 400 K, after which it was held constant for another 2 ns. For each tracer system, the final equilibrated positions and velocities were used as initial conditions for a production *NVE* run of 30 ns. Energy conservation was carefully verified. Typical energy drifts were found to be <1% per each 10 ns. Positions of all atoms were stored at least every 10 fs for analysis. The final frame of each *NVE* run was used as the initial condition for subsequent production runs of 30 ns in the *NVT* ensemble. Because diffusion constants were determined from our *NVE* calculations and viscosities from our *NVT* calculations, the temperature imposed in the latter was the ensemble average value of the *NVE* runs. The average temperature of our *NVE* runs was typically 5–12° above the nominal 400 K (Table S2 in the SI).

In all constant temperature calculations (*NpT* and *NVT*), the Nosé–Hoover<sup>48,49</sup> thermostat was used with relaxation time constants of 0.2 and 3.0 ps during equilibration and production phases, respectively. The Parrinello–Rahman barostat with a

coupling constant of 1.0 ps was employed in all constant pressure (*NpT*) runs. Equilibration and production runs for the neat liquid as well as four neutral tracer systems and four charged tracer systems accounted for  $\sim$ 600 ns of simulation time.

Experimental diffusion coefficients were measured following the same protocols described in ref 15. In brief, these measurements entailed pulsed field gradient  $^1\text{H}$  NMR using a Bruker AV-III-850 MHz NMR spectrometer with a Diff-30 probe, and the longitudinal-eddy-current delay stimulated echo pulse sequence with bipolar gradient pulse pairs.<sup>50</sup> Solutes were the highest quality available from Sigma-Aldrich and were used as received. The IL was prepared by Gary Baker as described in ref 51. Solutions 50 mM in solute were prepared by weight in dried IL and vacuum sealed in 5 mm NMR tubes. Experimentally and computationally derived tracer diffusion coefficients, molecular volumes, and friction ratios are provided in Tables S3 and S4 in the SI.

### 3. RESULTS AND DISCUSSION

For small neutral and charged tracers, we seek to develop a mechanistic interpretation of the deviation of  $\zeta_{\text{obs}}$  from  $\zeta_{\text{SE}}$  as the volume ratio between solute and solvent becomes small. In the case of solutes of the size of ammonium and methane, deviations in the frictional ratio  $\zeta_{\text{obs}}/\zeta_{\text{SE}}$  can reach 2 orders of magnitude. We therefore focus on these as our principal probes.

**3.1. Diffusion Mechanism of Small Charged and Neutral Tracers in Ionic Liquids.** In a set of recent high impact articles<sup>52–57</sup> the concept of non-Gaussian yet Brownian or Fickian diffusivity has been discussed. The basic idea is that a tracer probe undergoes simple Brownian diffusion but the underlying random walk step size is defined by characteristic non-Gaussian jumps on a much smaller time scale. At short times microscopic tracer dynamics are non-Gaussian, consisting of caging and escape events that underlie the coarser scale of time that defines the random walk. Perhaps the most interesting aspect of this perspective is that on the time scale when such cage and jump processes take place these are at the tails of the displacement probability distribution (the self Van Hove function<sup>58</sup>) of the probe defined in eq 2.

$$G_s^\alpha(r, t) = \frac{1}{N_\alpha} \left\langle \sum_i^{N_\alpha} \delta(r - |\mathbf{r}_i^\alpha(t_0) - \mathbf{r}_i^\alpha(t_1)|) \right\rangle_{t_0} \quad (2)$$

In eq 2,  $t = t_1 - t_0$  is the time difference,  $\delta$  is the delta function, and the angular brackets  $\langle \dots \rangle$  denote the ensemble average over time origins  $t_0$ . In most simple terms, events that could be rare even at short times can strongly influence Brownian dynamics at long times.

In our studies, the definition of short and long time scales very much depends on the size and charge of the tracer. Long time scales can simply be defined as times required to fully establish Fickian diffusive behavior. Probe-dependent short time scales are most conveniently defined by  $t^*$ , the time at which the non-Gaussian parameter  $\alpha_2(t)$ <sup>59,60</sup> (see eq 3) is maximum (i.e., the time scale when deviations from Gaussian tracer dynamics are most prominent). Plots of  $\alpha_2$  versus  $t$  as well as corresponding center of mass mean-square displacements are shown in Figures S4 and S5 in the SI.

$$\alpha_2(t) = \frac{3}{5} \frac{\langle r^4(t) \rangle}{\langle r^2(t) \rangle^2} - 1 \quad (3)$$

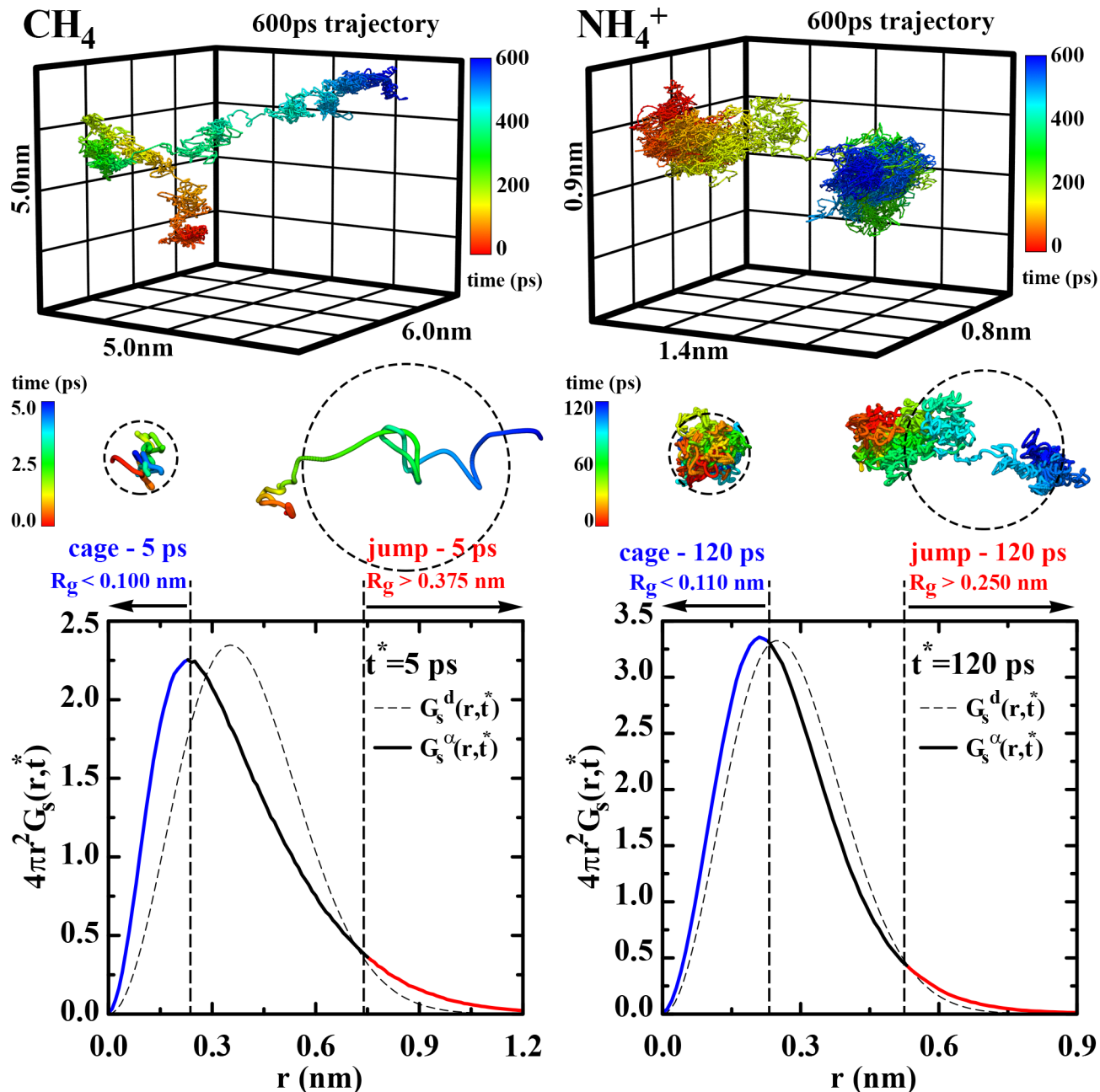


**Figure 2.** In the top panel, representative trajectory segments of 600 ps are shown for methane and ammonium tracers in the ionic liquid. To the right of the 3D trajectory plots are scales that associate the color code along the trajectory with time. In the middle panel, an example of cage and jump trajectory segments are extracted consistent with the time scale  $\Delta t = t^*$  corresponding to the maximum in the  $\alpha_2(t^*)$  parameter defined in the main text. For each type of tracer, the bottom panel shows the self Van Hove functions as well the corresponding ideal Gaussian distribution,  $G_s^d(r, t^*) = [3/2\pi\langle r^2(t^*) \rangle]^{3/2} \exp[-3r^2/2\langle r^2(t^*) \rangle]$ . Dashed vertical lines provide a definition of cage and jump segments associated with  $R^*$  in trajectory space, as explained in the main text.

The top portion of Figure 2 illustrates how considering different characteristic times for each solute is fundamentally important. On a 600 ps time scale, a trajectory for methane shows a sequence of several cage and jump segments, whereas ammonium has only a single jump region. It is with this probe-dependent microscopic time scale in mind that we move to establish a mechanistic relation between tracer dynamics, solute charge, solvent structure, and solvent dynamics.

**3.2. Relation Between Solute Dynamics and Ionic Liquid Structure.** To establish a working definition of tracer jump and cage regimes at  $t^*$  (each tracer has a different  $t^*$ ), we

first focus on deviations in the probability of displacements with respect to Gaussian behavior. In Figure 3,  $y = 0$  corresponds to Gaussian behavior. For all tracer probes three regions can be clearly distinguished: two regions, one at short displacements and one at long displacements with positive deviations (larger probability than expected), and one intermediate region with negative deviation (smaller probability than expected). The two regions with positive deviations define the cage and jump regimes. In one case, the probability of a tracer to stay put (caged) is larger than expected from Gaussian diffusion, and in the other the probability of tracers to move long distances

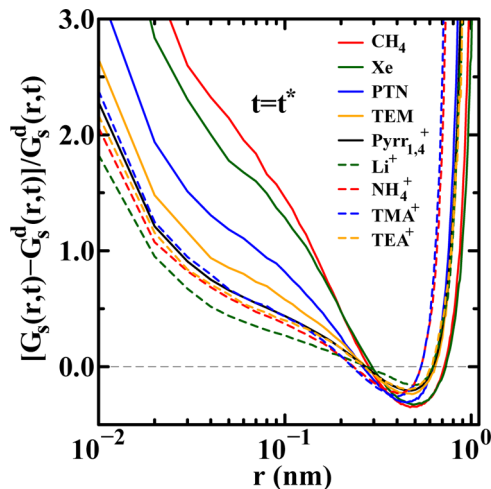


**Figure 3.** Comparison of  $[G_s^d(r,t) - G_s^d(r,t^*)]/G_s^d(r,t)$  versus  $r$  at time  $t = t^*$  corresponding to the non-Gaussian peak in the  $\alpha_2(t)$  parameter.

(jump) is exaggerated. This definition of cage and jump regimes is in a space of displacements defined by the self Van Hove correlation function.

To explore mechanistic aspects of diffusion in ILs, we seek a surrogate definition of cage and jump regimes not in displacement space but in trajectory space instead. In other words we want to identify trajectory segments of  $t^*$  duration that can be cataloged as in the cage or in the jump regimes. For this purpose, we think of a tracer trajectory in three dimensions in analogy to a long polymer with coiled (cage) regions and extended (jump) regions. We seek to explore in a statistical manner if these cage and jump regimes are correlated with IL structure. Accordingly we devise a statistical strategy based on the idea of the trajectory radius of gyration  $R_g^t$ . On this basis we define the characteristic size of a trajectory segment with time length  $\Delta t$  by the formula

$$R_{\Delta t}^g = \left[ \frac{1}{M_{\Delta t}} \sum_{j=1}^{M_{\Delta t}} (\mathbf{r}_j - \mathbf{r}_{gc})^2 \right]^{1/2} \quad (4)$$

where  $M_{\Delta t}$  is the number of time frames in a trajectory segment of length  $\Delta t = t_f - t_o$ ,  $\mathbf{r}_j$  is the coordinates of the solute's center of mass at frame  $j$ , and  $\mathbf{r}_{gc}$  is the coordinates of the geometrical center of the trajectory segment defined as

$$\mathbf{r}_{gc} = \frac{1}{M_{\Delta t}} \sum_{j=1}^M \mathbf{r}_j \quad (5)$$

The characteristic length scales of the cage and jump regimes can then be defined in terms of their  $R_{\Delta t}^g$ . For an unbiased comparison between different solutes,  $\Delta t$  in each case is chosen to be the characteristic time  $t^*$  where the non-Gaussian parameter  $\alpha_2(t)$  is maximal. This definition is reasonable because of the monotonically increasing trend between the self-diffusion constant of the tracer and the inverse of  $t^*$ , as shown in Figure S6 of the SI. Trajectories associated with the cage regime are here defined as having small  $2R_{\Delta t}^g$  toward the left side in Figure 3 consistent with positive deviations from the Gaussian distribution. In a like manner, the jump regime is defined as that where  $2R_{\Delta t}^g$  is large, corresponding to displacements that deviate positively from the Gaussian distribution toward the right side in Figure 3. Because  $R_{\Delta t}^g$

is a surrogate measure in trajectory space different from  $\langle r^2(\Delta t) \rangle^{1/2}$  in displacement space, the threshold definitions shown as vertical lines in the bottom panel of Figure 2 are somewhat arbitrary. In our study, these were chosen so that in each regime sufficient statistics could be collected for the calculation of correlation and pair distribution functions. The cutoffs are close to but not the same as the distances at which the ideal and real Van Hove functions intersect. An example of cage and jump trajectories segments associated with these cutoffs in the case of methane and ammonium is shown in the middle panel of Figure 2. Left and right panels of Figure 4 depict several other examples of cage and jump segments for methane and ammonium. It is clear from these representative examples that the surrogate definition in trajectory space as well as the cutoffs are doing what is expected—properly capturing jump and cage regimes in displacement space.

With this working definition of jump and cage trajectory segments that is clearly linked to tracer dynamical heterogeneity at  $t^*$  we proceed to address the fundamental question of whether tracer dynamical heterogeneity is associated with liquid structure. In other words, is fast and slow tracer diffusion the result of being in distinct and well-defined solvent environments or is it unrelated to solvent structure?

For the purpose of answering this question we focus on the ammonium and methane systems. These probes are of comparable sizes, and their positive and negative deviations from hydrodynamic behavior are significant. The results we present later are similar for other neutral and charged tracers, but the effects are less pronounced as the volume of the solute becomes larger. Effects are insignificant when the molecular volume of the tracer is larger than that of the solvent, as can be appreciated from Figure 1b.

The most intuitive way to address whether there is a connection between tracer dynamical heterogeneity and liquid structure is by plotting “trajectory-resolved” pair distribution functions. By trajectory-resolved we mean that we perform a separate analysis of tracer-solvent ensemble-averaged pair distribution functions during cage and jump trajectory segments. If the ensemble-averaged solute–solvent structure is different in the two trajectory types then a case can be made that a clear connection exists between fast or slow motion of the probe and solvation structure.

A compelling argument supporting the idea that solvent structure determines or at least strongly influences solute's translational dynamics can be derived from the upper panel in Figure 5. This panel shows trajectory-resolved pair correlation functions linking  $\text{CH}_4$ –cation–head,  $\text{CH}_4$ –anion, and  $\text{CH}_4$ –cation–tail centers of mass. We first notice that for the full trajectory the first solvation shell around methane contains cationic heads, tails, and anions in roughly similar proportions. (This can be corroborated from the integral of the pair distribution functions, Figure S7 in the SI). Cage pair distributions show that even in the case of a neutral solute such as methane, slow tracer dynamics is associated with solvation environments that have an excess density of cationic heads and anions when compared with the full trajectory. The opposite is true in the case of jump segments. Fast dynamics is correlated with a depletion in the first solvation shell of anionic and cationic-head density as compared with the full trajectory. In other words, local friction is enhanced if the neutral tracer is in an environment dominated by positive and negative charges and is diminished when a depletion of those occurs. Interestingly, because the tracer is neutral, this local friction

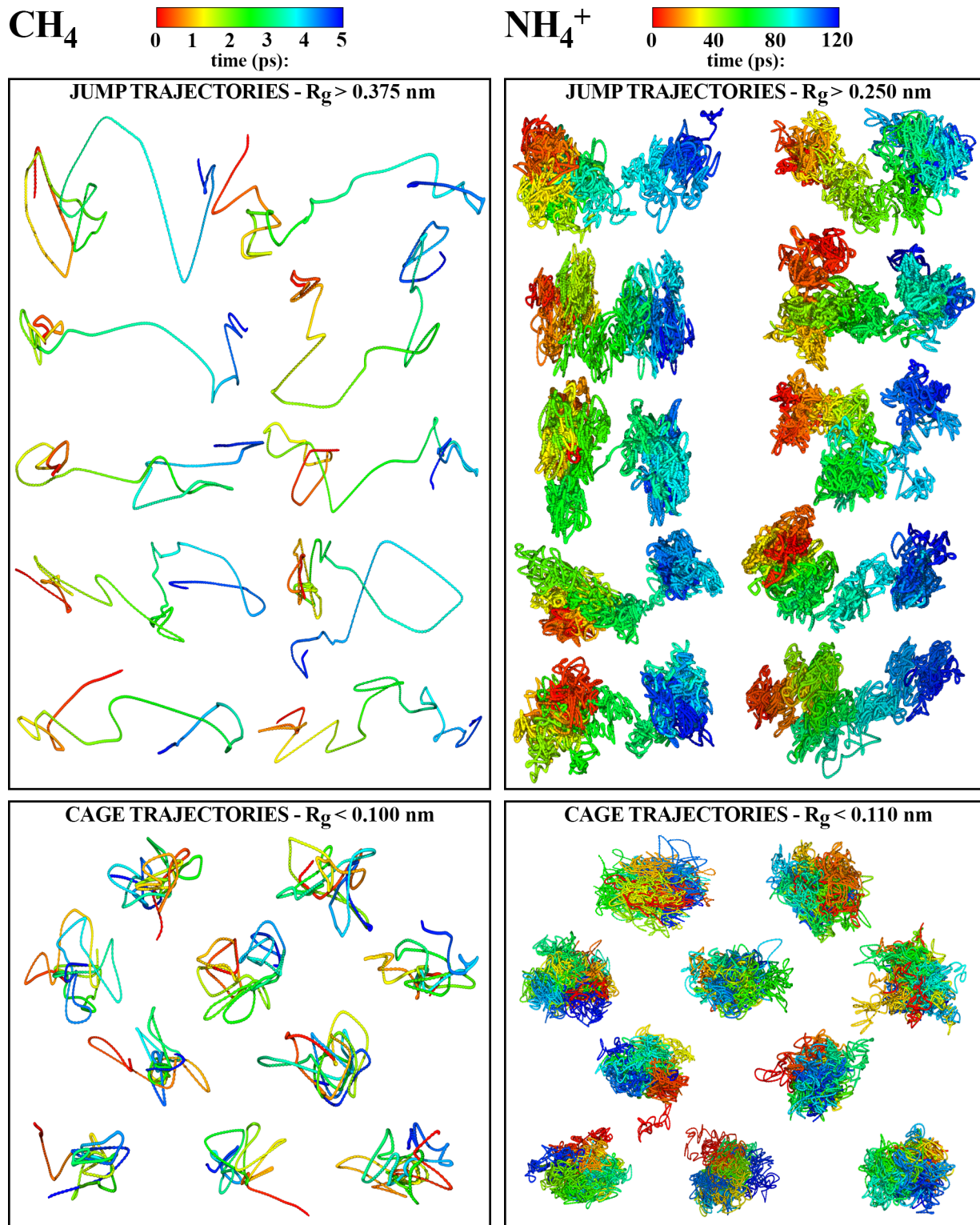


**Figure 4.** Examples of cage and jump trajectories for  $\text{CH}_4$  and  $\text{NH}_4^+$  in  $[\text{Pyrr}_{4,1}^+][\text{NTf}_2^-]$  showing how the cutoffs defined in Figure 2 for  $R_g^{\text{g}}$  in trajectory space properly capture short and long displacements that deviate positively from the ideal Gaussian distribution in displacement space.

effect should be mostly due to the local solvent stiffness (electrostriction effect<sup>61–63</sup>) and not due to tracer-solvent Coulombic interactions. As the tracer diffuses, it encounters regions that are stiff and regions that are soft. Stiff highly polar regions are associated with cage segments of the tracer trajectory, and soft and more apolar regions are associated with jump segments.

As conventional wisdom would dictate, in all cases tails are the component in closest contact with methane (see bottom panel in Figure S7 in the SI). Analyzing the solvation by tails we see that there is a small enhancement of tails in the jump regime compared with the cage regime. An integral of the pair distribution functions (Figure S7 in the SI) confirms that cage regimes are associated with extra heads around the tracer,

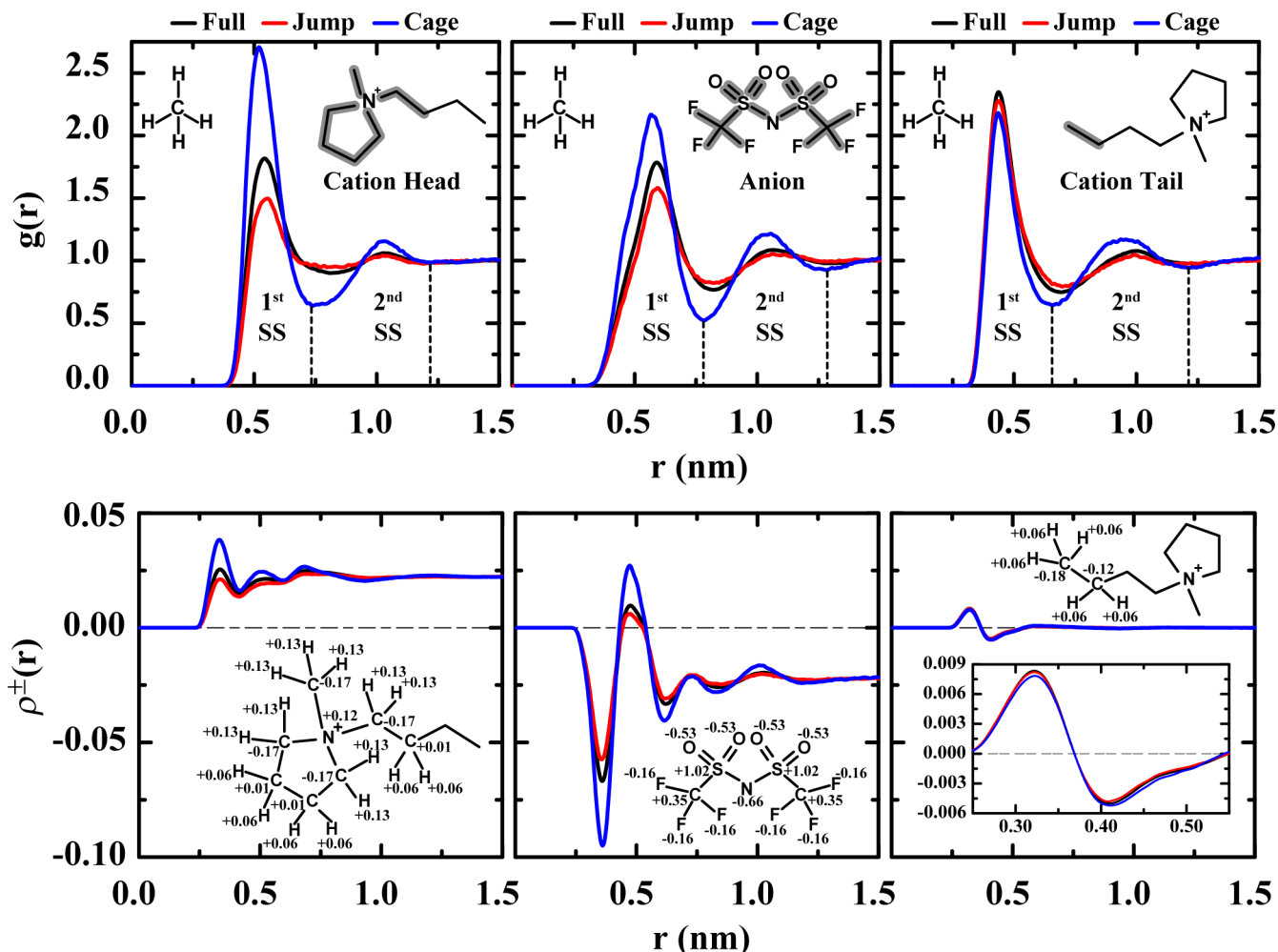


**Figure 5.** Trajectory-resolved radial distribution functions (top panel) and charge distribution functions (bottom panel) for  $\text{CH}_4$  with respect to the three main subcomponents of the IL solvent: cation tails, cation heads, and anions. On the top panel, the atoms included in each subcomponent are shown with a thick gray line on the chemical structure, whereas on the bottom panel the corresponding atomic charges are shown.

whereas the opposite is true in the case of jump regimes. We therefore conclude that, as probed by a small neutral tracer, stiff and soft solvent regions are unequivocally correlated with local polar or apolar solvent structure. One noticeable aspect in the analysis of cage segments is that the second peak of  $g(r)$  is always significantly more structured regardless of whether anions, cation heads, or cation tails are considered. This is consistent with the idea of caging occurring in locally stiff, charge-dominated, and highly organized solvent regions.

A more nuanced understanding of tracer solvation environments as they relate to local friction can be derived from trajectory-resolved charge density distribution functions. The lower panel in Figure 5 shows the distance-dependent solvent charge density around methane for cationic heads, anions, and cationic tails in the cage, jump, and full trajectory regimes. As would be expected, at longer distances the sum of cationic-head, cationic-tail, and anionic charge density components goes to zero independent of the type of trajectory segment. At short distances important differences can be detected when comparing jump and cage trajectory segments. In the case of cationic heads, positive charge density around the neutral solute is enhanced for cage segments and depleted with respect to the full trajectory in the case of jump segments. The same overall conclusion can be derived in the case of anions except that the

intramolecular anionic charge structure imposes negative and positive charge density oscillations. An enhancement of negative charge at contact with the neutral tracer is characteristic of cage segments and depletion of charge density with respect to the full trajectory occurs in jump regimes. In other words, fast methane diffusion is associated with soft local environments that are less polar, whereas cage regimes are associated with stiff polar environments.

The fast diffusion in these soft apolar environments significantly contributes to the negative deviations in the friction ratio plotted in Figure 1b. Reference 64 proposes a back-of-the-envelope calculation where the contribution of jump segments to the overall diffusion constant can be estimated in terms of  $R^6$ . Following a similar approach, we use the cutoffs in Figure 2 to establish a length scale  $\lambda$  for jumps. The number of jumps in a full trajectory is used to estimate a jump frequency,  $\nu$ . With both numbers, a jump-segment-only diffusion constant can be estimated as  $D_{\text{jumps}} = 1/6\nu\lambda^2$ .<sup>64</sup> In the case of methane, we find that the jump component, which is only ~5% of the overall trajectory, has a diffusion constant that is ~33% of that of the full trajectory. In other words, a small temporal fraction of the trajectory contributes to a large fraction of the overall displacement.

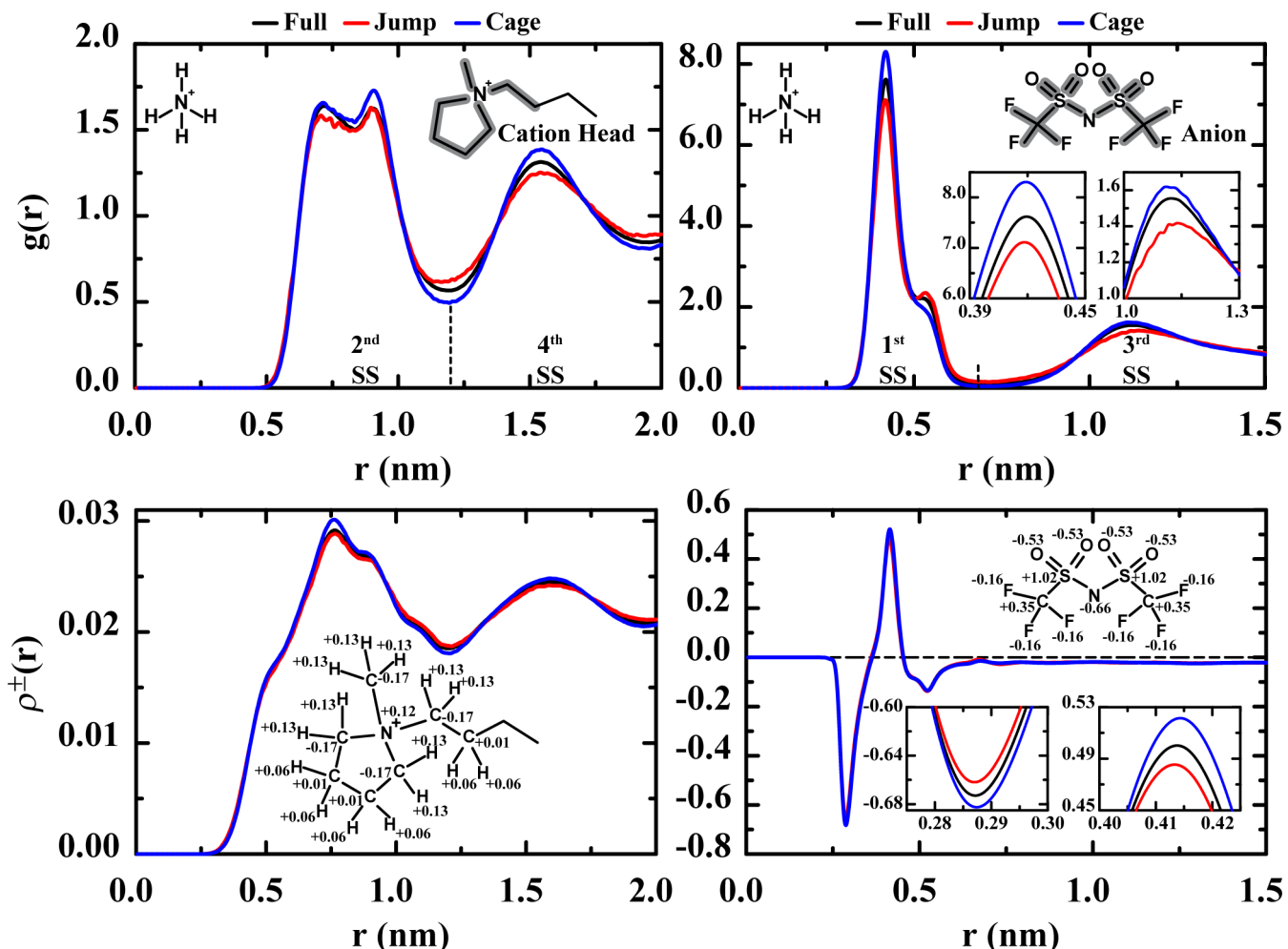


**Figure 6.** Trajectory-resolved radial distribution functions (top panels) and charge distribution functions (bottom panels) for  $\text{NH}_4^+$  with respect to cation heads and anions. On the top panel, the atoms included in each subcomponent are shown with a thick gray line on the chemical structure, whereas on the bottom panel the corresponding atomic charges are shown.

We now analyze the case of charged tracers. The upper right-hand panel of Figure 6 unsurprisingly shows that ammonium is at all times preferentially solvated by anions. The first anionic peak in the case of ammonium is much larger than the same peak in the case of methane. The tracer is an intrinsic component of the charged liquid network. Diffusion necessarily slows because of this. This is in stark contrast with, for example, experiments in which enhanced diffusivity of the lithium ion is achieved by complexation with glyme,<sup>65–67</sup> which diminishes anion trapping of the small charged solute. As opposed to the case of small neutral tracers, charge tracers couple to the positive and negative charges of the IL. If we think of small neutral solutes as innocent observers of soft and stiff solvent regions, we should instead consider small charged tracers as the source of a significant portion of the friction they experience due to charge–charge interactions with the solvent. In other words the tracer is an important source of the local electrostriction<sup>61</sup> that diminishes its own mobility.

A thorough understanding of mechanistic aspects pertaining to small charged tracer diffusion requires consideration of Figure 4. We first notice that jump segments defined by  $t^*$  are topologically different when comparing neutral and charged tracers of similar size. In the case of the neutral tracer, such segments look mostly elongated, whereas in the case of the charge tracer the topology of the trajectory looks more like a

dumbbell. This behavior is quite generic, as the right panel in Figure 4 shows. In other words, in the case of the charged tracer, jump segments defined by the time scale  $t^*$  include initial and final trapped regimes and an intermediate transition trajectory segment, during which the tracer quickly shuttles from one end of the dumbbell to the other. The fast shuttling mechanism between the two ends of the dumbbell often involves initial loss of a fraction of the tracer's anionic counterions, fast shuttling of the now smaller solvate across a mostly cationic solvation shell, and recovery of the missing anionic counterions at the other end of the dumbbell. Figure 7 shows a detailed example of this mechanism.

The upper panel in Figure 6 supports this analysis. Figure 6 (right panel) shows that for the full trajectory as well as the jump and cage segments, anions form the first solvation shell; however, when compared with the cage regime, the jump regime shows anionic depletion. This depletion is associated with the temporary loss and recovery of a counterion during the shuttling between dumbbell ends of jump segments. Notice that consistent with the idea of the loss of a first solvation shell anionic counterion, anionic depletion at contact in the jump regime is accompanied by the enhancement of a shoulder on the right-hand side of the first anionic peak in the pair distribution function at distances slightly larger than 0.5 nm.

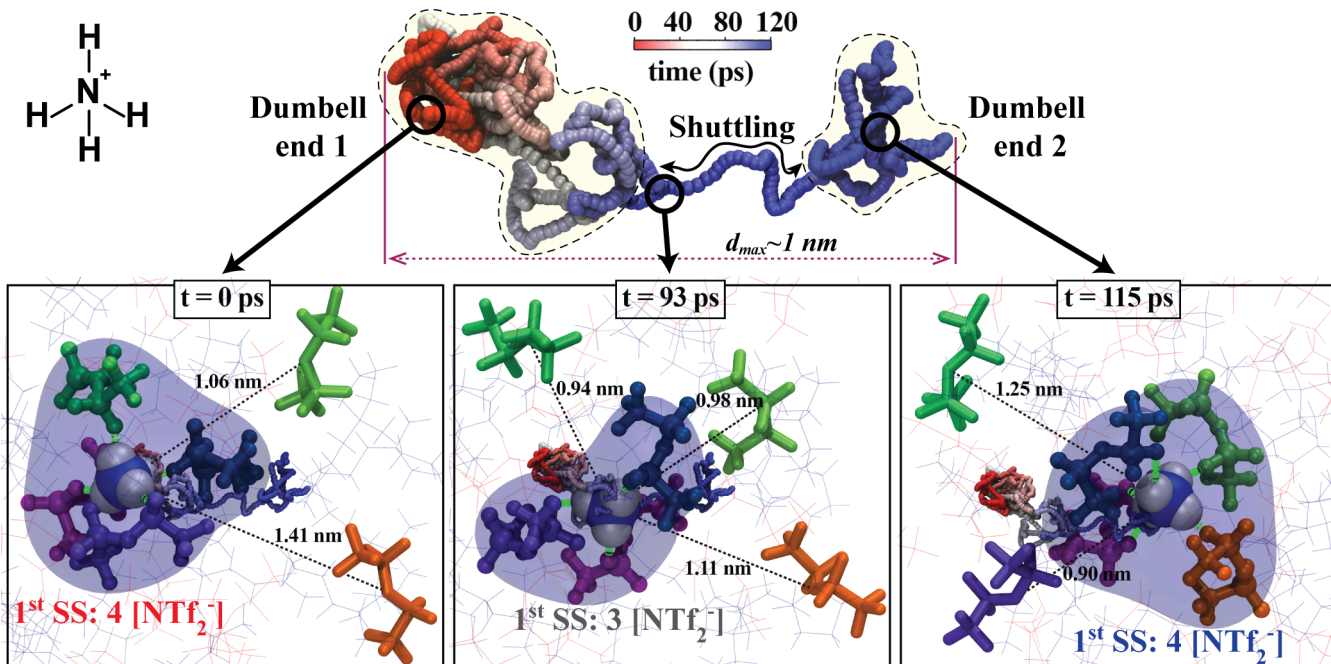


**Figure 7.** Topology of a dumbbell segment characteristic of the jump regime for ammonium in  $[\text{Pyrr}_{4,1}^+][\text{NTf}_2^-]$ . In the top panel we see a time color-coded trajectory segment highlighting the typical trap–shuttle–trap mechanism. In the bottom panel we see that the shuttle subsegment is associated with the loss of a fraction of the original anionic counterions and displacement of the defective solvate through a mostly cationic shell. In the final arrangement at the other end of the dumbbell, ammonium is solvated by a fraction of old (from the initial end of the dumbbell) and new (from the final end of the dumbbell) anionic counterions. In all trajectory snapshots depicted in the bottom panel, the translucent blue volume corresponds to the first anionic solvation shell. Hydrogen bonds to the tracer are shown with green lines, current snapshot first solvation shell anions are depicted in CPK format, and anions that are not in the first solvation shell but have been or will be are shown as licorice.

Cage-breaking events are the result of slightly looser (less structured) first through fourth solvation shells. The upper left panel in Figure 6 shows that in the cage regime the second and fourth solvation shells that are associated with the cationic component are better defined when compared with the full trajectory and the jump segments. The same conclusions can be derived from charge density distribution functions at the bottom of the same Figure. Initial and final cages associated with the ends of the dumbbell-like trajectory segments are separated by a distance consistent with a few  $\text{NH}_4^+$  diameters. This distance is short enough that anions in the first cage can easily participate in the final cage. A similar mechanism of hopping via anion exchange was proposed from MD simulations of  $\text{Li}^+$ -doped  $[\text{Pyrr}_{4,1}^+][\text{NTf}_2^-]$  with a polarizable force field.<sup>29,68</sup>

In summary, in the case of small charged tracers, diffusion is hindered because the solute is an intrinsic component of the charge network. A majority portion of the diffusion is of the solvate as a whole and not of the tracer alone. Jump regimes are associated with the breaking of a defective cage and the formation of a new one that shares a significant portion of the same counterions. Such mechanism is consistent with prior observations.<sup>68</sup> This enhanced local friction caused by constant anionic solvation even within jump segments is at the root of the positive deviations observed in Figure 1b for ammonium and other small positive tracers.

**3.3. Coupling Between Solute Dynamics and Ionic Liquid Dynamics.** So far we have focused our attention on the relation between tracer diffusion and IL structure. This section explores instead the time-dependent relaxation of solute–solvent pair distribution functions in the case of neutral and charged tracers using the same trajectory-resolved approach as

in Section 3.2. We seek to understand how solvent structure in the proximity of the tracer changes in time as charged and neutral tracer diffusion occurs in cage and jump regimes. What species occupy the space left vacant by the tracer? Does it depend on whether the tracer is neutral or charged?

This type of analysis is most naturally done in the context of the distinct Van Hove correlation function (eq 6) between species  $\alpha$  and  $\beta$ .<sup>58,60</sup> In this study,  $\alpha$  will always refer to the tracer and  $\beta$  to a subcomponent of interest in the solvent.

$$G_d^{\alpha\beta}(r, t) = \frac{N_\alpha + N_\beta}{N_\alpha N_\beta} \left\langle \sum_{i=1}^{N_\alpha} \sum_{j \neq i}^{N_\beta} \delta(r - |\mathbf{r}_i^\alpha(0) - \mathbf{r}_j^\beta(t)|) \right\rangle_{t_0} \quad (6)$$

The distinct Van Hove function measures the probability at time  $t$  of finding a particle of type  $\beta$  at a distance  $r$  from the location a particle of type  $\alpha$  occupied at  $t = 0$ . When  $t = 0$ , eq 6 is the pair distribution function ( $g^{\alpha\beta}(r)$ ); otherwise,  $G_d^{\alpha\beta}(r, t)$  simply measures the decay of  $g^{\alpha\beta}(r)$  with time. When  $t \rightarrow \infty$  or  $r \rightarrow \infty$ ,  $G_d^{\alpha\beta}(r, t) \rightarrow 1$ . This latter condition means that correlations between the solvent and the position where the tracer was initially located are lost at large distances or long times.

Whereas in section 3.2 we emphasized the role of the polar subcomponent of the IL in defining fast and slow motion of small neutral tracer molecules, here we will show that it is the cationic tails (the soft apolar subcomponent) that play a fundamental role in the coupling between neutral-solute and solvent dynamics. Figure 8 shows trajectory-resolved distinct Van Hove correlation functions in the case of methane solvated by different liquid subcomponents (cation heads, anions, and

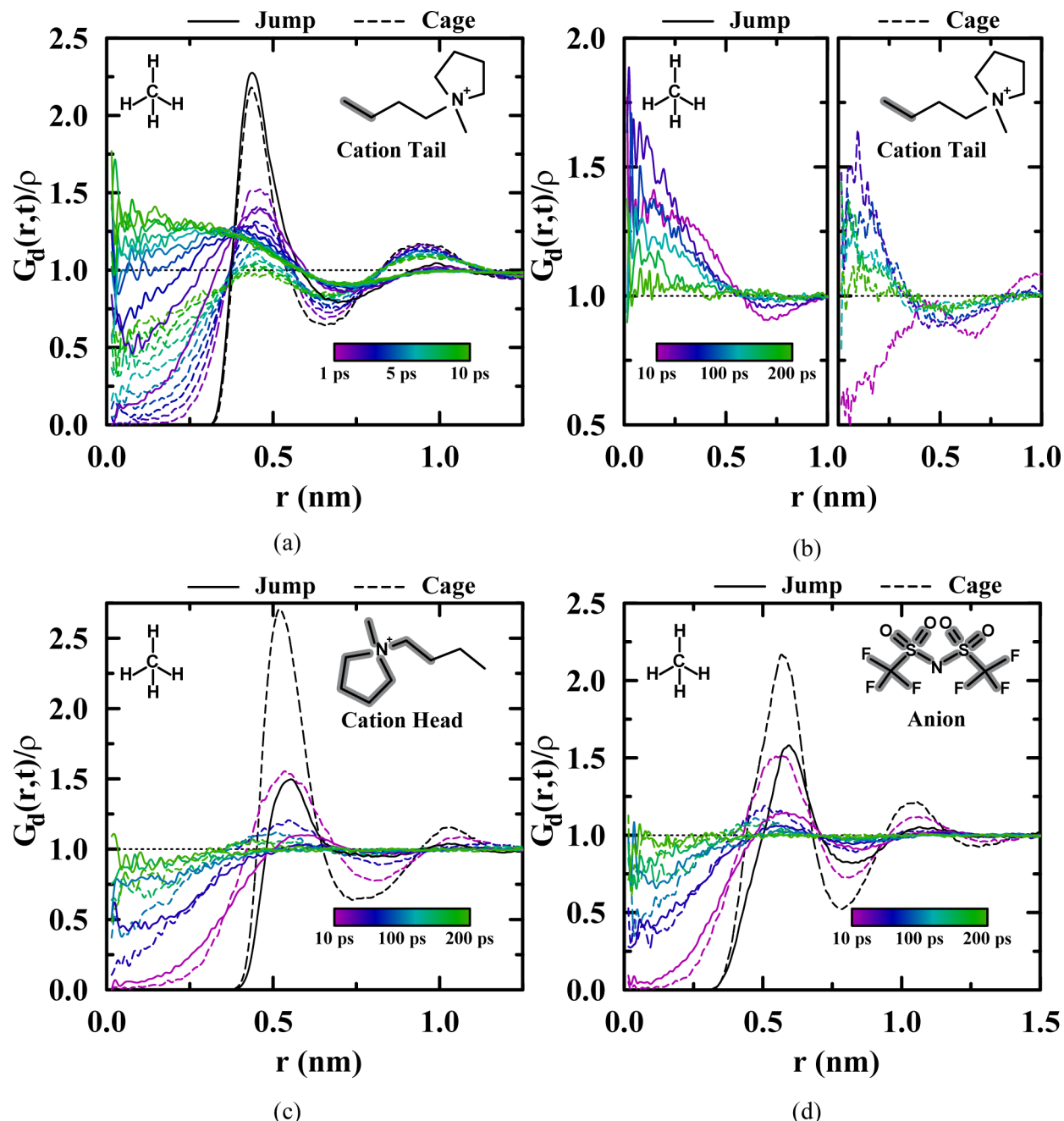


**Figure 8.** Trajectory-resolved distinct Van Hove correlation functions for  $\text{CH}_4$  with respect to the three main subcomponents of the IL solvent: cation tails at (a) short and (b) long time scales, (c) cation heads, and (d) anions. Color scales represent time scales of each distinct Van Hove curve, and black lines are the static RDFs.

cation tails). To analyze these Figures we will focus on two aspects; the first is how the space between  $r = 0$  and the first peak of the static pair distribution function  $g(r)$  (commonly referred as the “hole”) is filled by solvent as time evolves; the second is how peaks and troughs in  $g(r)$  morph.

We begin by analyzing the Van Hove correlation function between methane and cationic tails in Figures 8a,b. Functions are color-coded according to the time scale depicted in the insets. When looking at these graphs, the most salient feature is the difference in relaxation time scales associated with the “filling” of the hole at  $r = 0$ . For jump segments, the hole gets filled on a time scale of  $\sim 5$  ps, whereas for cage segments this occurs on a time scale an order of magnitude larger. This is a

simple consequence of the fact that in cage segments the solute moves from the origin on a much longer time scale. Notice that in the case of tails, “filling” implies going above  $G_d(r,t) = 1$  and then returning to one at long times. The physical interpretation is that liquid locations being vacated by the neutral solute are promptly filled by the apolar subcomponent of the solvent. In contrast, anions and cation heads fill the hole on a much longer time scale (Figures 8c,d), the same time scale on which all other features of the original  $g(r)$  are lost. Such behavior is a consequence of normal randomization at long times. Figure 9 illustrates the detailed mechanism of prompt hole filling by cationic tails. In the top panel, a jump time color-coded segment highlights two snapshots depicted at bottom right and

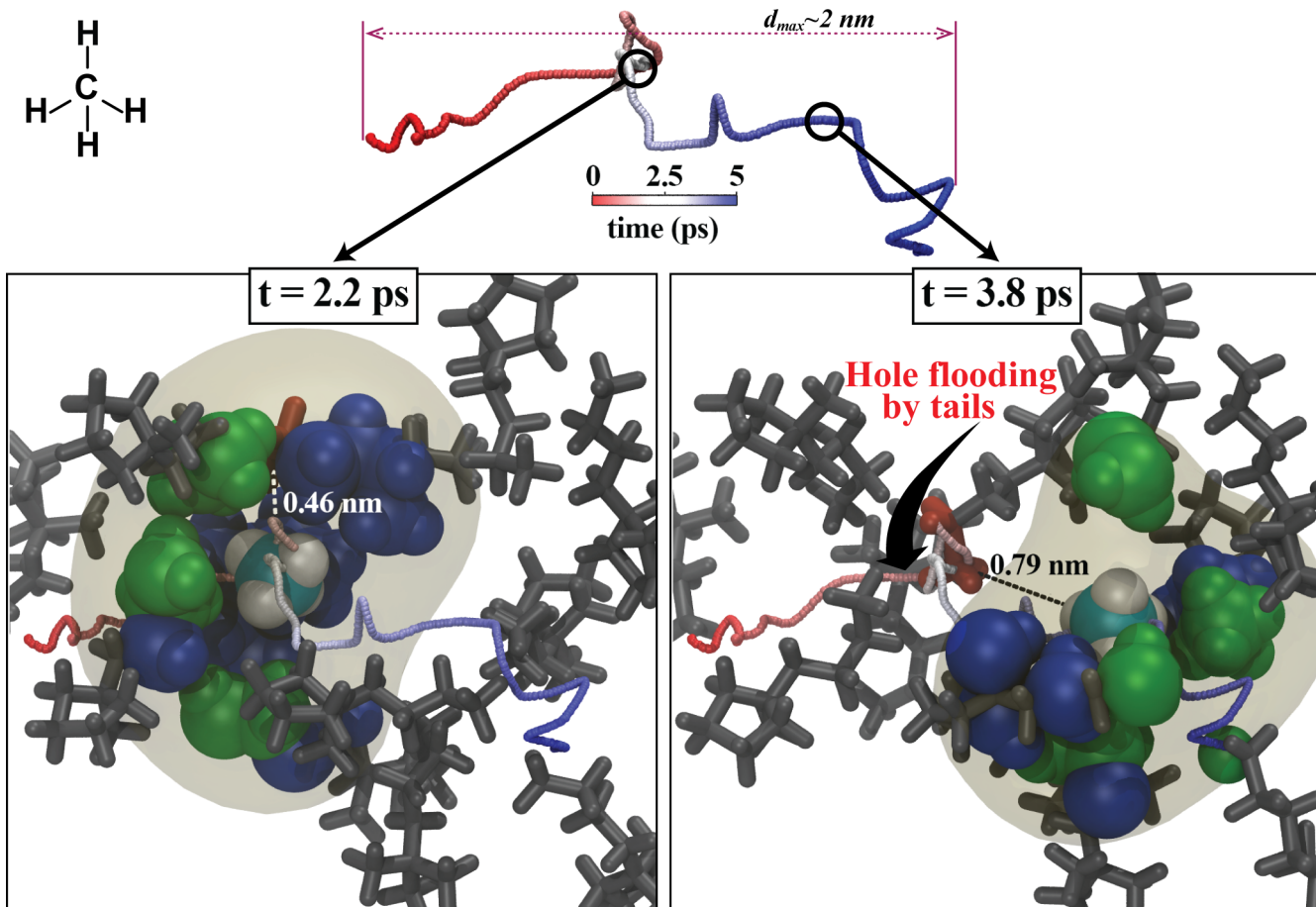


**Figure 9.** Top panel depicts a color-coded jump trajectory segment in the case of methane. Bottom panels depict two snapshots along the jump trajectory. Both snapshots include the full color-coded trajectory segment for easier reference. The snapshot on the left at 2.2 ps depicts in blue cationic heads and green cationic tails in close contact with methane. Other cations, which at some point during the segment come into close contact with the tracer, are depicted in gray licorice. The snapshot on the right uses the same color convention to show cationic components close to methane at 3.8 ps. The snapshot on the right highlights in brown licorice cationic tail components that occupy at this later time (3.8 ps) the location that methane originally occupied at 2.2 ps. This trajectory segment exemplifies the process of cationic tail flooding of the hole in the distinct Van Hove correlation function. In all cases, anions are omitted for clarity.

left. The snapshot on the left shows the location of cationic heads and tails surrounding methane at an earlier time. The snapshot on the right shows that after methane departs, its original location gets filled by cationic tails.

In contrast with what we observed in the case of tails for the neutral tracer, in the case of the small positively charged tracer it is the anions that initially flood the hole. Figure 10a,b shows Van Hove correlation functions between ammonium and the anionic subcomponent of the liquid. It is perhaps counter-intuitive that a cationic void would be filled by anions. What is happening is that the tracer is tightly solvated and it does not diffuse independently from its purely anionic first solvation shell. Because of this, if the tracer moves so do the anions that end up filling the position initially occupied by the tracer. This supports the mechanism exemplified in Figure 7, where ammonium moves with a fraction of its anionic counterions, which necessarily end up sweeping the locations formerly occupied by the tracer and flooding the hole in the Van Hove correlation function.

Unlike the anionic filling of the hole, Figure 10c,d shows that cationic subcomponents fill the hole on much longer time scales, only as all other memory of the tracer has been lost. At long times we notice that cationic components appear to fill the

hole in a convex manner. This hints at a possible same-charge ion-exchange mechanism that should be further explored.

#### 4. DISCUSSION AND CONCLUSIONS

When the molecular volume of a solute tracer is small compared with that of the solvent it is naturally expected that deviations from SE behavior will occur. In fact, it is surprising how well theories purely based on a single viscosity parameter work all the way from the macroscopic solute limit to the limit, in which solute and solvent are of comparable sizes. In an IL when a neutral tracer solute is small, it necessarily experiences local regions of higher and lower charge concentration than the average. If a tracer is neutral and does not strongly couple to the charged environments, the effect is that it experiences regions that are locally stiff (of high liquid charge density) and locally soft (of low electrostriction). This causes a strong coupling between liquid structure and probe dynamics. Stiff and soft environments may also be at the origin of the type of energetic heterogeneity described in ref 69.

The IL in this study,  $[\text{Pyrr}_{4,1}^+][\text{NTf}_2^-]$  was chosen so that structural heterogeneity in the form of apolar and charged domains was suppressed. There is no first sharp diffraction peak (or prepeak), the most obvious signature of nanoscale polar

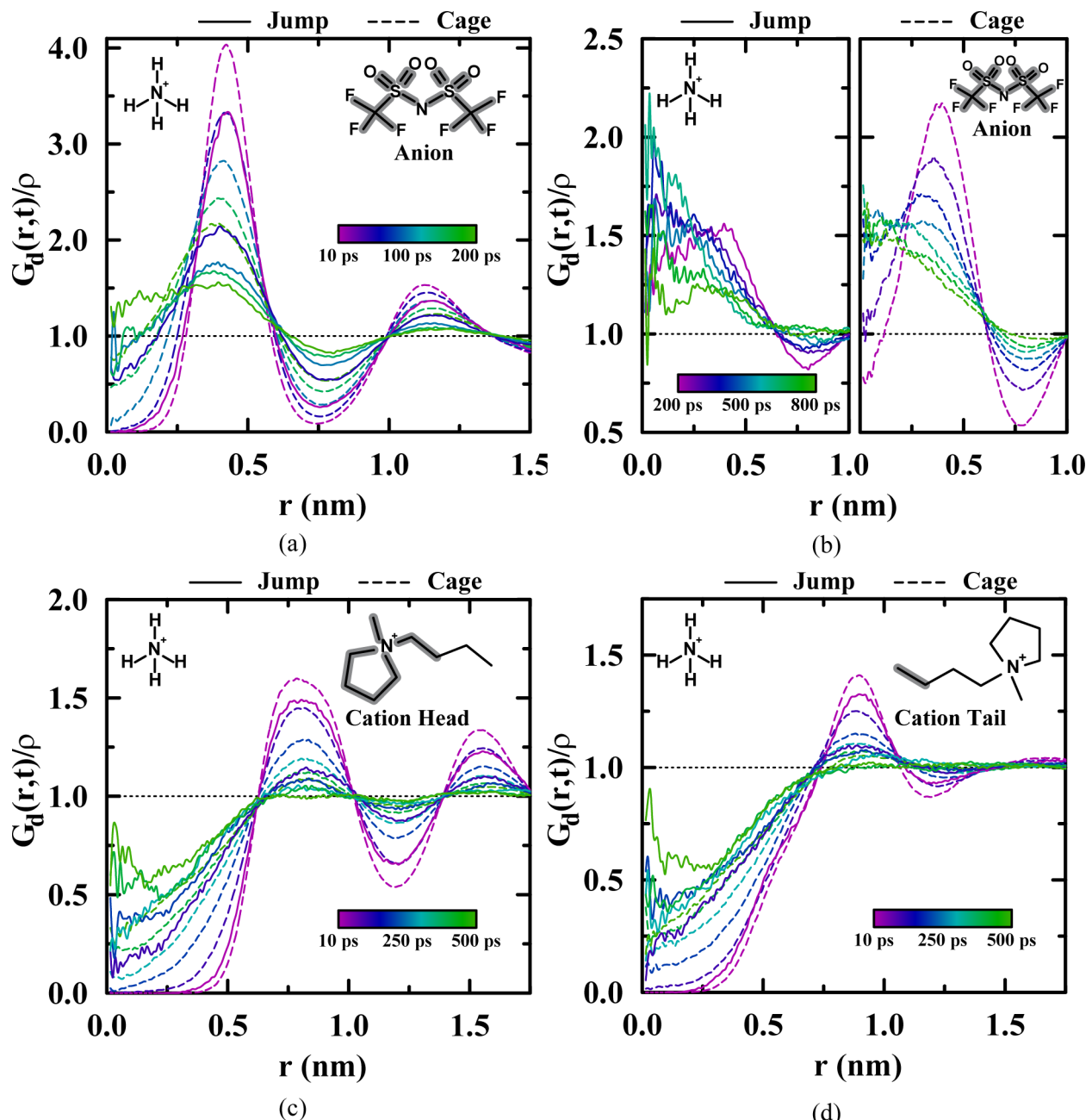


**Figure 10.** Trajectory-resolved distinct Van Hove correlation functions for  $\text{NH}_4^+$  with respect to the three main subcomponents of the IL solvent: anions at (a) short and (b) long time scale, (c) cation heads, and (d) cation tails. Color scales represent the time ranges of each distinct Van Hove curve.

and apolar alternation, in this IL. Nonetheless, we have found that for a neutral probe more polar regions are associated with caging trajectory segments, whereas regions that are less polar are associated with fast diffusive jump segments. It is possible that this behavior will be much more pronounced in liquids with significant apolar environments. If this is indeed the case, what we are describing would result in the link between structural heterogeneity and dynamical heterogeneity that has been extensively discussed but not yet corroborated in the room-temperature ILs literature. Work on such systems is currently underway in our laboratories.

The overall effect of the fast incursions of neutral probes through the less polar portion of the liquid is a negative deviation from unit of the ratio of the observed versus SE

friction. In simple terms, the diffusion of small neutral solutes slows in charged regions and speeds in more apolar regions. The overall result when viewed on a longer scale of time and on a coarser scale of length is a random walk where the step size is strongly influenced by the speedy incursions in the less polar region. In the case of methane the deviation in the friction ratio is on the order of 1 to 2 orders of magnitude. For smaller atomic gases in the same liquid or for gases of the size of methane in ILs with larger molecular volume the departure from hydrodynamic predictions is even larger.<sup>15</sup>

From a structural perspective, the charged component of the liquid plays a significant role in the caging of neutral solutes; however, from a dynamical perspective it is the apolar tails of the cation that are most significantly coupled to the diffusion of

the solute. The strong dynamical coupling between a small neutral tracer and the tails of the cation can be seen from the filling of the hole at  $r = 0$  in the solute–solvent distinct Van Hove correlation function. When the solute diffuses away from the origin, it is the apolar tails of the cations that promptly flood the location where the neutral probe was originally. Time reversal symmetry of the Van Hove function dictates (and our simulations confirm) that the same mechanism is at play at the other end of the diffusive process, where it is tails that move out of the way for the solute to access new locations. In other words, in the case of neutral solutes it is the soft component of the liquid that is also the most mobile and the one that is coupled to the motion of the tracer.

Small charged probes exhibit deviations from the SE expected friction opposite to that of neutral tracers. In this case, the solute strongly couples to the charges of the solvent ions and is not an innocent spectator of stiff and soft solvent regions but instead a participant in creating the electrostriction it experiences. Because cations in low-viscosity ILs are often asymmetric and large, it is expected that a small positively charged tracer ion will interact with anions even more strongly than the solvent cations do. At larger solute concentrations this results in severe increases in solution viscosity.<sup>29,70–74</sup>

Small ionic tracers become an intrinsic component of the network of charge in the IL. It is not appropriate to think of the tracer as diffusing independently. Even the idea of solvates or solvent-bergs appears to be an oversimplification, as anions in the first solvation shell of the probe are also solvating other cationic components of the liquid. During jump trajectory segments it is often defective solvates that move in a concerted form. Some anions in the first solvation shells are lost, some are conserved, and some new ones are added at the end of jump trajectory segments. The persistent jamming of the tracer in charged regions of the solvent results in diffusion consistent with a friction larger than expected from the bulk viscosity.

In conclusion, we argue that although the transient nature of the solute–solvent local dynamics is dissipated in the Brownian limit, its cumulative effect shapes long-term diffusion. This is certainly not unique to ILs. What is unique about ILs is their ionic and apolar structure. This article shows that this structural duality (and likely dynamical duality) strongly correlates with slow and fast modes of tracer diffusion.

## ASSOCIATED CONTENT

### Supporting Information

Model and force field parameters, tracer and solvent self-diffusivity, IL solvent structure, solvent viscosity and solute effects, experimental tracer diffusion coefficients, computational tracer diffusion coefficients, tracer diffusivity and non-Gaussian characteristic time, and trajectory-resolved radial distribution functions and their number integral. This material is available free of charge via the Internet at <http://pubs.acs.org>.

## AUTHOR INFORMATION

### Corresponding Author

\*E-mail: claudio-margulis@uiowa.edu

### Notes

The authors declare no competing financial interest.

## ACKNOWLEDGMENTS

This material is based on work supported by the U.S. Department of Energy, Office of Basic Energy Sciences,

Division of Chemical Sciences, Geosciences, and Biosciences under contracts DE-SC0008644 and DE-FG02-12ER16363 awarded to C.J.M. and M.M., respectively. J.C.A. and C.J.M. also acknowledge a generous allocation of high performance computational resources provided by The University of Iowa.

## REFERENCES

- (1) Gorlov, M.; Kloo, L. Ionic Liquid Electrolytes for Dye-Sensitized Solar Cells. *Dalton Trans.* **2008**, *20*, 2655–2666.
- (2) Manthiram, A.; Fu, Y.; Chung, S.-H.; Zu, C.; Su, Y.-S. Rechargeable Lithium-Sulfur Batteries. *Chem. Rev.* **2014**, *114*, 11751–11787.
- (3) Hapiot, P.; Lagrost, C. Electrochemical reactivity in room-temperature ionic liquids. *Chem. Rev.* **2008**, *108*, 2238–2264.
- (4) Parvulescu, V. I.; Hardacre, C. Catalysis in Ionic Liquids. *Chem. Rev.* **2007**, *107*, 2615–2665.
- (5) Hallett, J. P.; Welton, T. Room-Temperature Ionic Liquids: Solvents for Synthesis and Catalysis. 2. *Chem. Rev.* **2011**, *111*, 3508–3576.
- (6) Chiappe, C.; Pieraccini, D. Ionic liquids: solvent properties and organic reactivity. *J. Phys. Org. Chem.* **2005**, *18*, 275–297.
- (7) Castner, E. W., Jr.; Margulis, C. J.; Maroncelli, M.; Wishart, J. F. Ionic Liquids: Structure and Photochemical Reactions. *Annu. Rev. Phys. Chem.* **2011**, *62*, 85–105.
- (8) Visser, A.; Swatloski, R.; Reichert, W.; Mayton, R.; Sheff, S.; Wierzbicki, A.; Davis, J.; Rogers, R. Task-specific ionic liquids for the extraction of metal ions from aqueous solutions. *Chem. Commun.* **2001**, *135*–136.
- (9) de los Ríos, A. P.; Hernández-Fernández, F. J.; Lozano, L. J.; Sánchez, S.; Moreno, J. I.; Godínez, C. Removal of Metal Ions from Aqueous Solutions by Extraction with Ionic Liquids. *J. Chem. Eng. Data* **2010**, *55*, 605–608.
- (10) Vrentas, J. S.; Duda, J. L. Molecular diffusion in polymer solutions. *AICHE J.* **1979**, *25*, 1–24.
- (11) Evans, D. F.; Tominaga, T.; Chan, C. Diffusion of symmetrical and spherical solutes in protic, aprotic, and hydrocarbon solvents. *J. Solution Chem.* **1979**, *8*, 461–478.
- (12) Fujita, H. Diffusion in polymer-diluent systems. *Adv. Polym. Sci.* **1961**, *3/1*, 1–47.
- (13) Cicerone, M. T.; Blackburn, F.; Ediger, M. Anomalous diffusion of probe molecules in polystyrene: evidence for spatially heterogeneous segmental dynamics. *Macromolecules* **1995**, *28*, 8224–8232.
- (14) Cicerone, M. T.; Ediger, M. D. Enhanced translation of probe molecules in supercooled o-terphenyl: Signature of spatially heterogeneous dynamics? *J. Chem. Phys.* **1996**, *104*, 7210–7218.
- (15) Kaintz, A.; Baker, G.; Benesi, A.; Maroncelli, M. Solute Diffusion in Ionic Liquids, NMR Measurements and Comparisons to Conventional Solvents. *J. Phys. Chem. B* **2013**, *117*, 11697–11708.
- (16) Kaintz, A.; Baker, G.; Benesi, A.; Maroncelli, M. Correction to “Solute Diffusion in Ionic Liquids, NMR Measurements and Comparisons to Conventional Solvents. *J. Phys. Chem. B* **2014**, *118*, 5615–5615.
- (17) Vorotnytsev, M. A.; Zinov'yeva, V. A.; Picquet, M. Diffusional transport in ionic liquids: Stokes-Einstein relation or “sliding sphere” model? Ferrocene (Fc) in imidazolium liquids. *Electrochim. Acta* **2010**, *55*, 5063–5070.
- (18) McLean, A.; Muldoon, M.; Gordon, C.; Dunkin, I. Bimolecular rate constants for diffusion in ionic liquids. *Chem. Commun.* **2002**, 1880–1881.
- (19) Skrzypczak, A.; Neta, P. Diffusion-Controlled Electron-Transfer Reactions in Ionic Liquids. *J. Phys. Chem. A* **2003**, *107*, 7800–7803.
- (20) Grodkowski, J.; Neta, P.; Wishart, J. F. Pulse radiolysis study of the reactions of hydrogen atoms in the ionic liquid methyltributylammonium bis[(trifluoromethyl)sulfonyl]imide. *J. Phys. Chem. A* **2003**, *107*, 9794–9799.
- (21) Vieira, R. C.; Falvey, D. E. Photoinduced Electron-Transfer Reactions in Two Room-Temperature Ionic Liquids: 1-Butyl-3-

- methylimidazolium Hexafluorophosphate and 1-Octyl-3-methylimidazolium Hexafluorophosphate. *J. Phys. Chem. B* **2007**, *111*, 5023–5029.
- (22) Paul, A.; Samanta, A. Photoinduced Electron Transfer Reaction in Room Temperature Ionic Liquids: A Combined Laser Flash Photolysis and Fluorescence Study. *J. Phys. Chem. B* **2007**, *111*, 1957–1962.
- (23) Sarkar, S.; Pramanik, R.; Seth, D.; Setua, P.; Sarkar, N. Photoinduced electron transfer (PET) from N,N-dimethylaniline to 7-amino Coumarin dyes in a room temperature ionic liquid (RTIL): Slowing down of electron transfer rate compared to conventional solvent. *Chem. Phys. Lett.* **2009**, *477*, 102–108.
- (24) Liang, M.; Kaintz, A.; Baker, G. A.; Maroncelli, M. Bimolecular Electron Transfer in Ionic Liquids: Are Reaction Rates Anomalously High? *J. Phys. Chem. B* **2012**, *116*, 1370–1384.
- (25) Gordon, C.; McLean, A. Photoelectron transfer from excited-state ruthenium(II) tris(bipyridyl) to methylviologen in an ionic liquid. *Chem. Commun.* **2000**, 1395–1396.
- (26) Grodkowski, J.; Neta, P. Formation and Reaction of Br<sub>2</sub><sup>•-</sup> Radicals in the Ionic Liquid Methyltributylammonium Bis-(trifluoromethylsulfonyl)imide and in Other Solvents. *J. Phys. Chem. A* **2002**, *106*, 11130–11134.
- (27) Wishart, J. F.; Neta, P. Spectrum and Reactivity of the Solvated Electron in the Ionic Liquid Methyltributylammonium Bis-(trifluoromethylsulfonyl)imide. *J. Phys. Chem. B* **2003**, *107*, 7261–7267.
- (28) Takahashi, K.; Sakai, S.; Tezuka, H.; Hiejima, Y.; Katsumura, Y.; Watanabe, M. Reaction between Diiodide Anion Radicals in Ionic Liquids. *J. Phys. Chem. B* **2007**, *111*, 4807–4811.
- (29) Solano, C. J. F.; Jeremias, S.; Paillard, E.; Beljonne, D.; Lazzaroni, R. A joint theoretical/experimental study of the structure, dynamics, and Li<sup>+</sup> transport in bis([tri]fluoro[methane]sulfonyl)imide [T]FSI-based ionic liquids. *J. Chem. Phys.* **2013**, *139*, 034502.
- (30) Edward, J. T. Molecular Volumes and Stokes-Einstein Equation. *J. Chem. Educ.* **1970**, *47*, 261.
- (31) Kashyap, H. K.; Hettige, J. J.; Annapureddy, H. V. R.; Margulis, C. J. SAXS anti-peaks reveal the length-scales of dual positive-negative and polar-apolar ordering in room-temperature ionic liquids. *Chem. Commun.* **2012**, *48*, 5103–5105.
- (32) Santos, C. S.; Murthy, N. S.; Baker, G. A.; Castner, E. W., Jr. Communication: X-ray scattering from ionic liquids with pyrrolidinium cations. *J. Chem. Phys.* **2011**, *134*, 121101.
- (33) Russina, O.; Triolo, A.; Gontrani, L.; Caminiti, R. Mesoscopic Structural Heterogeneities in Room-Temperature Ionic Liquids. *J. Phys. Chem. Lett.* **2012**, *3*, 27–33.
- (34) Russina, O.; Triolo, A. New experimental evidence supporting the mesoscopic segregation model in room temperature ionic liquids. *Faraday Discuss.* **2012**, *154*, 97–109.
- (35) Jorgensen, W. L.; Maxwell, D. S.; Tirado-Rives, J. Development and Testing of the OPLS All-Atom Force Field on Conformational Energetics and Properties of Organic Liquids. *J. Am. Chem. Soc.* **1996**, *118*, 11225–11236.
- (36) Canongia Lopes, J. N.; Pádua, A. A. H. Molecular Force Field for Ionic Liquids Composed of Triflate or Bistriflylimide Anions. *J. Phys. Chem. B* **2004**, *108*, 16893–16898.
- (37) Canongia Lopes, J. N. A.; Pádua, A. A. H. Nanostructural Organization in Ionic Liquids. *J. Phys. Chem. B* **2006**, *110*, 3330–3335.
- (38) Köddermann, T.; Paschek, D.; Ludwig, R. Molecular dynamic simulations of ionic liquids: A reliable description of structure, thermodynamics and dynamics. *ChemPhysChem* **2007**, *8*, 2464–2470.
- (39) Morrow, T. I.; Maginn, E. J. Molecular Dynamics Study of the Ionic Liquid 1-n-Butyl-3-methylimidazolium Hexafluorophosphate. *J. Phys. Chem. B* **2002**, *106*, 12807–12813.
- (40) Tokuda, H.; Ishii, K.; Susan, M. A. B. H.; Tsuzuki, S.; Hayamizu, K.; Watanabe, M. Physicochemical Properties and Structures of Room-Temperature Ionic Liquids. 3. Variation of Cationic Structures. *J. Phys. Chem. B* **2006**, *110*, 2833–2839.
- (41) Hess, B.; Kutzner, C.; Van Der Spoel, D.; Lindahl, E. GROMACS 4: Algorithms for Highly Efficient, Load-Balanced, and Scalable Molecular Simulation. *J. Chem. Theory Comput.* **2008**, *4*, 435–447.
- (42) Van Der Spoel, D.; Lindahl, E.; Hess, B.; Groenhof, G.; Mark, A. E.; Berendsen, H. J. C. GROMACS: Fast, flexible, and free. *J. Comput. Chem.* **2005**, *26*, 1701–1718.
- (43) Van Gunsteren, W.; Berendsen, H. A leap-frog algorithm for stochastic dynamics. *Mol. Simul.* **1988**, *1*, 173–185.
- (44) Darden, T.; York, D.; Pedersen, L. Particle mesh Ewald: An N log(N) method for Ewald sums in large systems. *J. Chem. Phys.* **1993**, *98*, 10089–10092.
- (45) Essmann, U.; Perera, L.; Berkowitz, M. L.; Darden, T.; Lee, H.; Pedersen, L. G. A smooth particle mesh Ewald method. *J. Chem. Phys.* **1995**, *103*, 8577–8593.
- (46) Hess, B. P-LINCS: A parallel linear constraint solver for molecular simulation. *J. Chem. Theory Comput.* **2008**, *4*, 116–122.
- (47) Hess, B.; Bekker, H.; Berendsen, H. J.; Fraaije, J. G. LINCS: a linear constraint solver for molecular simulations. *J. Comput. Chem.* **1997**, *18*, 1463–1472.
- (48) Nosé, S. A unified formulation of the constant temperature molecular dynamics methods. *J. Chem. Phys.* **1984**, *81*, 511–519.
- (49) Nosé, S. A molecular dynamics method for simulations in the canonical ensemble. *Mol. Phys.* **1984**, *52*, 255–268.
- (50) Wu, D. H.; Chen, A. D.; Johnson, C. S. An Improved Diffusion-ordered Spectroscopy Experiment Incorporating Bipolar-gradient Pulses. *J. Magn. Reson., Ser. A* **1995**, *115*, 260–264.
- (51) Jin, H.; O'Hare, B.; Dong, J.; Arzhantsev, S.; Baker, G. A.; Wishart, J. F.; Benesi, A. J.; Maroncelli, M. Physical properties of ionic liquids consisting of the 1-butyl-3-methylimidazolium cation with various anions and the bis(trifluoromethylsulfonyl)imide anion with various cations. *J. Phys. Chem. B* **2008**, *112*, 81–92.
- (52) Guan, J.; Wang, B.; Granick, S. Even Hard-Sphere Colloidal Suspensions Display Fickian Yet Non-Gaussian Diffusion. *ACS Nano* **2014**, *8*, 3331–3336.
- (53) Wang, B.; Anthony, S. M.; Bae, S. C.; Granick, S. Anomalous yet Brownian. *Proc. Natl. Acad. Sci. U.S.A.* **2009**, *106*, 15160–15164.
- (54) Wang, B.; Kuo, J.; Bae, S. C.; Granick, S. When Brownian diffusion is not Gaussian. *Nat. Mater.* **2012**, *11*, 481–485.
- (55) Kwon, G.; Sung, B. J.; Yethiraj, A. Dynamics in Crowded Environments: Is Non-Gaussian Brownian Diffusion Normal? *J. Phys. Chem. B* **2014**, *118*, 8128–8134.
- (56) Kim, J.; Kim, C.; Sung, B. J. Simulation Study of Seemingly Fickian but Heterogeneous Dynamics of Two Dimensional Colloids. *Phys. Rev. Lett.* **2013**, *110*, 047801.
- (57) Chaudhuri, P.; Berthier, L.; Kob, W. Universal nature of particle displacements close to glass and jamming transitions. *Phys. Rev. Lett.* **2007**, *99*, 060604.
- (58) Van Hove, L. Correlations in Space and Time and Born Approximation Scattering in Systems of Interacting Particles. *Phys. Rev.* **1954**, *95*, 249–262.
- (59) Rahman, A. Correlations in the motion of atoms in liquid argon. *Phys. Rev.* **1964**, *136*, A405.
- (60) Kob, W.; Andersen, H. C. Testing mode-coupling theory for a supercooled binary Lennard-Jones mixture I: The van Hove correlation function. *Phys. Rev. E: Stat., Nonlinear, Soft Matter Phys.* **1995**, *51*, 4626.
- (61) Kumar, P. V.; Maroncelli, M. The non-separability of “dielectric” and “mechanical” friction in molecular systems: A simulation study. *J. Chem. Phys.* **2000**, *112*, 5370–5381.
- (62) Shim, Y.; Choi, M. Y.; Kim, H. J. A molecular dynamics computer simulation study of room-temperature ionic liquids. I. Equilibrium solvation structure and free energetics. *J. Chem. Phys.* **2005**, *122*, 44510.
- (63) Shim, Y.; Choi, M. Y.; Kim, H. J. A molecular dynamics computer simulation study of room-temperature ionic liquids. II. Equilibrium and nonequilibrium solvation dynamics. *J. Chem. Phys.* **2005**, *122*, 44511.
- (64) Raptis, T. E.; Raptis, V. E.; Samios, J. New Effective Method for Quantitative Analysis of Diffusion Jumps, Applied in Molecular

Dynamics Simulations of Small Molecules Dispersed in Short Chain Systems. *J. Phys. Chem. B* **2007**, *111*, 13683–13693.

(65) Tamura, T.; Hachida, T.; Yoshida, K.; Tachikawa, N.; Dokko, K.; Watanabe, M. New glyme-cyclic imide lithium salt complexes as thermally stable electrolytes for lithium batteries. *J. Power Sources* **2010**, *195*, 6095–6100.

(66) Mandai, T.; Yoshida, K.; Ueno, K.; Dokko, K.; Watanabe, M. Criteria for solvate ionic liquids. *Phys. Chem. Chem. Phys.* **2014**, *16*, 8761–8772.

(67) Tsuzuki, S.; Shinoda, W.; Matsugami, M.; Umebayashi, Y.; Ueno, K.; Mandai, T.; Seki, S.; Dokko, K.; Watanabe, M. Structures of [Li (glyme)]<sup>+</sup> complexes and their interactions with anions in equimolar mixtures of glymes and Li[TFSA]: analysis by molecular dynamics simulations. *Phys. Chem. Chem. Phys.* **2015**, *17*, 126–129.

(68) Haskins, J. B.; Bennett, W. R.; Wu, J. J.; Hernandez, D.; Borodin, O.; Monk, J. D.; Bauschlicher, C. W.; Lawson, J. W. Computational and Experimental Investigation of Li-doped Ionic Liquid Electrolytes: [pyr14][TFSI], [pyr13][FSI], and [EMIM][BF4]. *J. Phys. Chem. B* **2014**, *118*, 11295–11309.

(69) Zhao, Y.; Hu, Z. *Chem. Commun.* **2012**, *48*, 2231–2233.

(70) Tsuzuki, S.; Hayamizu, K.; Seki, S. Origin of the Low-Viscosity of [emim][(FSO<sub>2</sub>)<sub>2</sub>N] Ionic Liquid and Its Lithium Salt Mixture: Experimental and Theoretical Study of Self-Diffusion Coefficients, Conductivities, and Intermolecular Interactions. *J. Phys. Chem. B* **2010**, *114*, 16329–16336.

(71) Hayamizu, K.; Tsuzuki, S.; Seki, S.; Fujii, K.; Suenaga, M.; Umebayashi, Y. Studies on the translational and rotational motions of ionic liquids composed of N-methyl-N-propyl-pyrrolidinium ( $P_{13}$ ) cation and bis(trifluoromethanesulfonyl)amide and bis(fluorosulfonyl)amide anions and their binary systems including lithium salts. *J. Chem. Phys.* **2010**, *133*, 194505.

(72) Liu, H.; Maginn, E. Effect of ion structure on conductivity in lithium-doped ionic liquid electrolytes: A molecular dynamics study. *J. Chem. Phys.* **2013**, *139*, 114508.

(73) Lawler, C.; Fayer, M. D. The Influence of Lithium Cations on Dynamics and Structure of Room Temperature Ionic Liquids. *J. Phys. Chem. B* **2013**, *117*, 9768–9774.

(74) Fujii, K.; Hamano, H.; Doi, H.; Song, X.; Tsuzuki, S.; Hayamizu, K.; Seki, S.; Kameda, Y.; Dokko, K.; Watanabe, M.; Umebayashi, Y. Unusual Li<sup>+</sup> Ion Solvation Structure in Bis(fluorosulfonyl)amide Based Ionic Liquid. *J. Phys. Chem. C* **2013**, *117*, 19314–19324.